Amplitude-dependent topological edge states in nonlinear phononic lattices

Raj Kumar Pal,[1,*] Javier Vila,[1] Michael Leamy,[2] and Massimo Ruzzene[1,2]
[1]*School of Aerospace Engineering, Georgia Institute of Technology, Atlanta, Georgia 30332, USA*
[2]*School of Mechanical Engineering, Georgia Institute of Technology, Atlanta, Georgia 30332, USA*

(Received 3 May 2017; revised manuscript received 31 October 2017; published 21 March 2018)

This work investigates the effect of nonlinearities on topologically protected edge states in one- and two-dimensional phononic lattices. We first show that localized modes arise at the interface between two spring-mass chains that are inverted copies of each other. Explicit expressions derived for the frequencies of the localized modes guide the study of the effect of cubic nonlinearities on the resonant characteristics of the interface, which are shown to be described by a Duffing-like equation. Nonlinearities produce amplitude-dependent frequency shifts, which in the case of a softening nonlinearity cause the localized mode to migrate to the bulk spectrum. The case of a hexagonal lattice implementing a phononic analog of a crystal exhibiting the quantum spin Hall effect is also investigated in the presence of weakly nonlinear cubic springs. An asymptotic analysis provides estimates of the amplitude dependence of the localized modes, while numerical simulations illustrate how the lattice response transitions from bulk-to-edge mode-dominated by varying the excitation amplitude. In contrast with the interface mode of the first example studies, this occurs both for hardening and softening springs. The results of this study provide a theoretical framework for the investigation of nonlinear effects that induce and control topologically protected wave modes through nonlinear interactions and amplitude tuning.

DOI: 10.1103/PhysRevE.97.032209

I. INTRODUCTION

Wave propagation in periodic media is an active field of research with applications in diverse areas of science and engineering. Phononic crystals allow superior wave manipulation and control compared to conventional bulk media, since they present directional band gaps and highly anisotropic dynamic behavior. Potential applications include vibration control, surface acoustic wave devices, and wave steering [1]. Recently, the achievement of defect-immune and scattering-free wave propagation using periodic media has received significant attention. The advent of topological mechanics [2] provides an effective framework for the pursuit of robust wave propagation, which is protected against perturbations and defects. Topologically protected edge wave propagation was originally envisioned in quantum systems and it has been quickly extended to other classical areas of physics, including acoustic [3], photonic [4], optomechanical [5], and elastic [6,7] media. The unique properties achieved in these media, such as immunity to backscattering and localization in the presence of defects and imperfections, are a result of band topology. These properties allow for lossless propagation of information, or waves confined to a boundary or interface. Therefore, they may be part of a fundamentally new mechanism for wave-based transport of information or energy.

There are two broad ways to realize topologically protected wave propagation in elastic media. The first one uses active components, thereby mimicking the quantum Hall effect. Changing the parity of active devices or modulating the physical properties in time have been shown to alter the direction and nature of edge waves [8,9]. Examples include magnetic fields in biological systems [10], rotating disks [11], and acoustic circulators operating on the basis of a flow-induced bias [12]. The second way uses solely passive components and relies on establishing analogs of the quantum spin Hall effect. These media feature both forward- and backward-propagating edge modes, which can be induced by an external excitation of appropriate polarization. The concept is illustrated in several studies by way of both numerical [6,7,13,14] and experimental [15,16] investigations, which involve coupled pendulums [15], plates with two scale holes [6] and resonators [7], as well as electric circuits [16]. Numerous studies have also been conducted on localized nonpropagating deformation modes at the interface of two structural lattices [7,17,18]. These modes depend on the topological properties of the bands, and in one-dimensional (1D) lattices they are characterized by the Zak phase as the topological invariant [19]. In 2D and 3D lattices, several researchers have investigated the presence of floppy modes of motion due to nontrivial topological polarization and exploited these modes to achieve localized buckling and directional response [20–23].

While most studies consider systems governed by linear interactions, there is growing interest in the investigation of the effect of nonlinearities in topological materials. Nonlinearities, for example, enable tunable wave motion, which in turn may lead to nonreciprocal wave propagation [24,25]. This finds potential applications in acoustic switching [26], diodes [27], and delay lines [28]. Nonlinear effects have been investigated to demonstrate self-induced topological phase transitions in the Su-Schrieffer-Heeger (SSH) model [29]. In the field of photonics, several studies have considered topological effects in nonlinear media. Included in these studies are solitonlike topological states, which exist on the edges of weakly nonlinear

*raj.pal@aerospace.gatech.edu

photonic systems [30–32]. These solitons arise in systems that can be described by a nonlinear Schrödinger (NLS) equation [30–33] and coupled nonlinear SSH equations [34], all obtained from a Kerr-like optical nonlinearity.

This work investigates the effect of nonlinearities on two types of topologically protected localized modes in phononic lattices. Specifically, we study the robustness and frequency content of localized modes in 1D and 2D lattices. In the 1D lattice, we illustrate the amplitude-dependent resonant behavior of an interface mode, which can lead to its shifting into the bulk bands. In the 2D case, the perturbation approach of [35,36] is applied to predict the amplitude-dependent frequency of edge modes for both hardening and softening springs. In both cases, the predictions are verified through numerical simulations on finite lattices excited by forces of increasing amplitude.

The outline of this paper is as follows: Sec. II presents a discrete 1D lattice (chain) with an interface and explicit expressions for the frequency and mode shapes of modes localized at the interface. The corresponding tunable nonlinear chain version is discussed in Sec. II B. Then in Sec. III we show how the lattice response can switch from bulk to edge waves at a fixed frequency by varying the amplitude in a 2D lattice. The 2D designs are verified by a combination of dispersion analysis and numerical simulations on finite lattices. Finally, Sec. IV presents the conclusions of this study.

II. INTERFACE MODES IN A 1D LATTICE

We begin our investigations by illustrating the existence and behavior of interface modes in a 1D spring-mass chain. The linear case is presented first in order to briefly describe the existence of localized modes at the interface of chains that are characterized by distinct topological invariants, which in this case is the Zak phase [19,37]. The analytical derivation of the interface mode frequencies is presented in Appendix A, and details of the topological properties of the linear chain are provided in Appendix B. Next, the behavior of an interface with nonlinear interactions is investigated in detail through its representation as a simple, single degree of freedom oscillator. This approach enables the study of the effect of nonlinearities in relation to the existence of the interface mode as a function of the excitation amplitude, and specifically to its tendency to enter the bulk spectrum based on the parameters defining the nonlinear interactions.

A. Linear chain: Analytical and numerical results

The spring-mass chain model considered is displayed in Fig. 1. It consists of two sublattices, each with identical masses and having alternating springs with stiffness k_1 and k_2 and of an interface (or defect) mass connecting them. The interface mass is connected to springs with stiffness k_1 on both sides. The unit cells on the right and left of this interface are inverted copies of each other. This discrete lattice was investigated in [7], where the existence of two types of localized modes was discussed.

The governing equation for the free vibration of interface mass is

$$m\ddot{u}_{c,0} + k_1(2u_{c,0} - u_{b,0} - u_{b,1}) = 0. \tag{1}$$

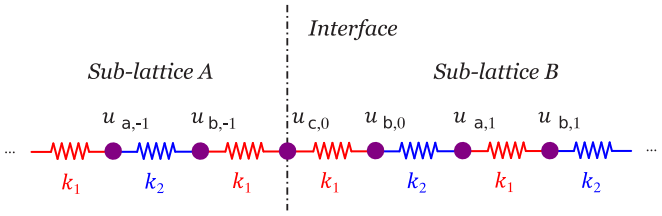

FIG. 1. Two sublattices (A and B), which are inverted copies of each other, are joined together. The interface supports a localized mode in the band-gap frequencies.

Similarly, the governing equations for a unit cell p of the sublattice on the left of the interface are

$$m\ddot{u}_{a,p} + k_2(u_{a,p} - u_{b,p}) + k_1(u_{a,p} - u_{b,p-1}) = 0, \tag{2a}$$

$$m\ddot{u}_{b,p} + k_2(u_{b,p} - u_{a,p}) + k_1(u_{b,p} - u_{a,p+1}) = 0, \tag{2b}$$

while for a unit cell p on the right sublattice they are

$$m\ddot{u}_{a,p} + k_1(u_{a,p} - u_{b,p}) + k_2(u_{a,p} - u_{b,p-1}) = 0, \tag{3a}$$

$$m\ddot{u}_{b,p} + k_1(u_{b,p} - u_{a,p}) + k_2(u_{b,p} - u_{a,p+1}) = 0. \tag{3b}$$

The above equations are normalized by writing the spring constants as $k_1 = k(1+\gamma)$ and $k_2 = k(1-\gamma)$, with γ being a stiffness parameter and k being the mean stiffness. A nondimensional time scale $\tau = \sqrt{k/m}t$ is introduced to express the equations in nondimensional form.

In the present work, explicit expressions for the frequency of the localized modes at the interface are derived by using a transfer-matrix approach. The derivations can be found in Appendix A. These expressions allow us to identify and investigate the parameters affecting the frequency and mode shapes in a systematic way. They also shed light on the amplitude dependence (for $\gamma < 0$) and independence (for $\gamma > 0$) of the localized modes in chains with weakly nonlinear springs. Our theoretical predictions are verified through a combination of frequency domain analysis and transient numerical simulations on a finite chain with an interface.

The following are the solutions for the frequencies that support localized solutions:

$$\begin{aligned} &\gamma < 0: \quad \Omega = \sqrt{3 - \sqrt{1 + 8\gamma^2}}, \quad \text{antisymmetric mode,} \\ &\gamma > 0: \quad \Omega = \sqrt{2}, \quad \text{symmetric mode,} \\ &\gamma > 0: \quad \Omega = \sqrt{3 + \sqrt{1 + 8\gamma^2}}, \quad \text{antisymmetric mode.} \end{aligned} \tag{4}$$

Here Ω is the dimensionless frequency obtained by normalizing with the reference frequency $\sqrt{k/m}$. The detailed derivations of these frequencies along with their associated mode shapes are presented in Appendix A. Note that the first and second solutions give frequencies that are localized in the band gap between the acoustic and optical branches, while the

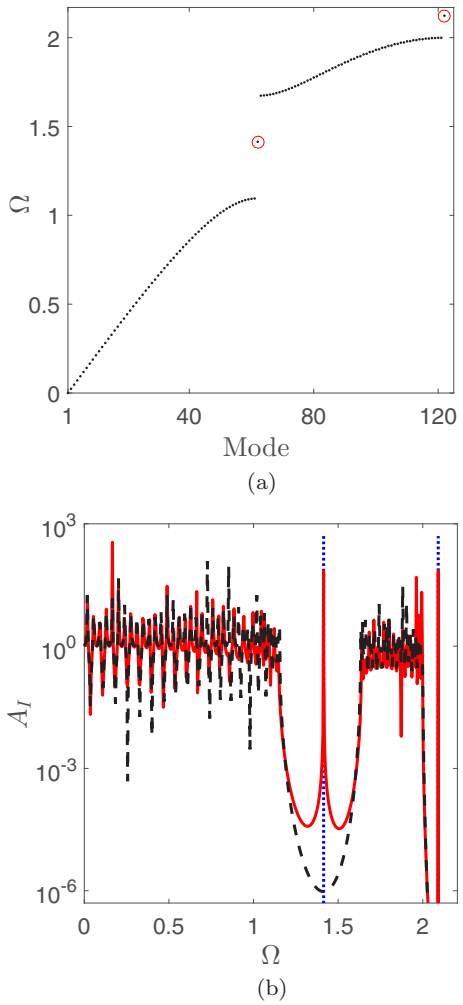

FIG. 2. (a) Natural frequencies of a finite chain exhibiting interface modes (red circles) in the band-gap frequencies. (b) Frequency response function [solid (red) line] showing the interface mode within the band gap, in agreement with analytical predictions [dotted (blue) line]. Interface modes are absent in a regular chain with all identical unit cells [dashed (black) line].

third frequency is above the optical branch. Furthermore, the first and third frequencies are associated with antisymmetric mode shapes where the unit cells on both sides of the interface are in phase, while the second frequency is associated with a symmetric mode shape, with the interface mass being at rest, while the unit cells on both sides have a phase difference of π.

We verify our analytical predictions by numerically computing the modes of oscillation of a finite chain having 60 unit cells with an interface at the center; see Fig. 1. The stiffness parameter is set to $\gamma = 0.4$. The governing equations for our lattice may be written in matrix form as $\boldsymbol{M}\ddot{\boldsymbol{q}}(\tau) + \boldsymbol{K}\boldsymbol{q}(\tau) = \boldsymbol{f}(\tau)$. We seek the forced vibration response of the linear chain when subjected to an external force $\boldsymbol{f}\cos\Omega\tau$. Imposing a solution ansatz of the form $\boldsymbol{q}(\tau) = \boldsymbol{q}e^{i\Omega\tau}$, the governing equation reduces to

$$(\boldsymbol{K} - \Omega^2\boldsymbol{M})\boldsymbol{q} = \boldsymbol{f}. \tag{5}$$

Figure 2(a) displays the natural frequencies Ω of this chain, obtained by solving the eigenvalue problem that arises by setting $\boldsymbol{f} = \boldsymbol{0}$. It illustrates the presence of a band gap between the acoustic and optical modes. Furthermore, there is an interface mode in the band gap at frequency $\Omega = \sqrt{2}$, which matches exactly with the analytical solution of Ω_i for $\gamma > 0$ in Eq. (A8). Analogous results are obtained for the chain with $\gamma < 0$, consistent with the analytical expressions for the localized mode frequencies and shapes.

To illustrate the dynamic behavior of this chain, we compute the frequency response function by imposing a displacement $u_{b,30} = \cos(\Omega\tau)$ on the mass at the left boundary. The other end of the chain is free and the frequency response is normalized with the excitation amplitude, which is unity in our study. We also consider a chain that has no interface and comprises 60 identical unit cells (regular chain), in which edge modes are not expected. Figure 2(b) displays the displacement amplitude of the center mass for both chains obtained by solving Eq. (5) with appropriate displacement boundary conditions ($\boldsymbol{f} = \boldsymbol{0}$) over a wide frequency range. In the band-gap frequency range, the regular chain with all identical unit cells does not support any resonance mode. The chain with an interface mass has a resonance mode, consistent with the analytical solution [Eq. (A8)].

1. Reduced model for forced response

We now seek the forced vibration response of a chain comprised of N unit cells on each side of the interface. The interface mass is subjected to an external forcing f at frequency Ω. We consider the antisymmetric mode that arises when $\gamma < 0$, for which we derive a reduced order model when the interface mass is subjected to the external force. As shown in Eq. (A8), the interface mode is antisymmetric, i.e., $u_{b,0} = u_{b,-1}$. Since the wave number is π in the band gaps and there is no propagation, this displacement relation is valid for frequencies in the band gap when $\gamma < 0$. The relation $\boldsymbol{u}_N = \boldsymbol{T}^N\boldsymbol{u}_0$ can be inverted to get the relation $\boldsymbol{u}_0 = \boldsymbol{T}^{-N}\boldsymbol{u}_N$. We reduce the chain to a single degree of freedom system that governs the behavior of the interface mass, and we obtain an expression for the effective stiffness on the interface mass. Fixing the first and last masses of the chain ($u_{b,N} = u_{b,-N} = 0$), the relation $\boldsymbol{u}_0 = \boldsymbol{T}^{-N}\boldsymbol{u}_N$ simplifies to the equation $u_{b,0}/S_{12} = u_{c,0}/S_{11}$, where S_{ij} are the components of $\boldsymbol{S} = \boldsymbol{T}^{-N}$. The governing equation of the interface mass is $[2(1+\gamma) - \Omega^2]u_{c,0} - 2(1+\gamma)u_{b,0} = f$. Eliminating $u_{b,0}$ from these two relations yields the following expression for the effective behavior of the interface mass:

$$\left[2(1+\gamma)\left(1 - \frac{S_{21}}{S_{11}}\right) - \Omega^2\right]u_{c,0} = f. \tag{6}$$

Explicit expressions for the terms S_{11} and S_{21} in terms of the excitation frequency Ω and γ are presented in Appendix C.

The results for the interface frequency can be further generalized to the case of springs adjacent to the interface different from k_1 through a parameter χ. The springs connected to the interface mass are changed to χk_1 while the stiffness of all the other springs in the chain remains unchanged. Figure 3(a) illustrates a schematic of this modified interface. The governing equation for the interface mass now becomes

$$-\Omega^2 u_{c,0} + \chi(1+\gamma)(2u_{c,0} - u_{b,0} + u_{b,-1}) = 0.$$

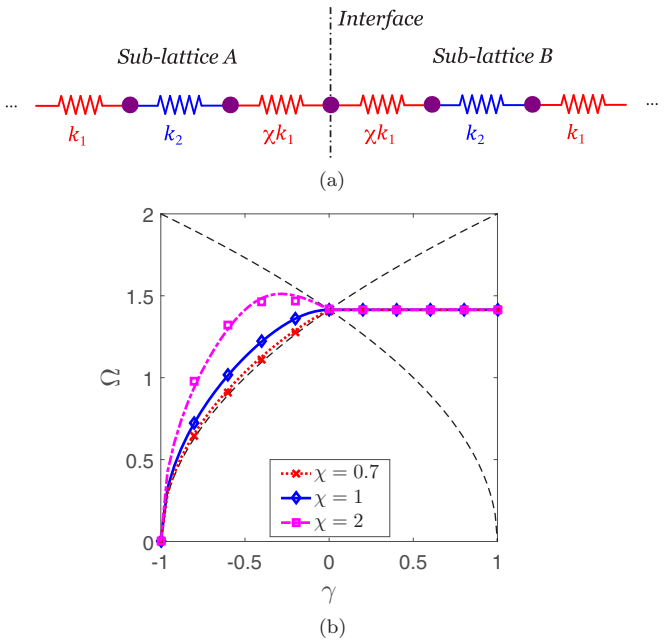

FIG. 3. (a) Schematic of an interface having springs with modified stiffness χk_1. All other spring stiffnesses remain unchanged. (b) Variation of the interface frequency as a function of γ for the three distinct values of χ listed in the legend. Dashed curves show frequencies bounding the band gap.

Numerical analysis is performed to determine the natural frequencies of this modified interface using a chain of 60 unit cells by solving the eigenvalue problem [$\boldsymbol{f} = \boldsymbol{0}$ in Eq. (5)]. The interface mode frequency is located by examining its corresponding mode shape. Figure 3(b) displays the interface mode frequency for three distinct χ values: 0.7, 1, and 2 over a range of stiffness parameter values γ. Also shown by dashed lines are the frequencies bounding the band gap. We observe that only the antisymmetric mode ($\gamma < 0$) frequency shifts, while the symmetric mode ($\gamma > 0$) frequency remains unchanged. This surprising observation can be explained by examining the mode shape of the edge mode when $\gamma > 0$. For this mode shape, the interface mass $(c,0)$ has zero displacement as the forces acting on its either side are equal and opposite. Thus changing the stiffness of the spring connecting $(c,0)$ from both sides does not affect the dynamic behavior of this mass. The displacements of the adjacent masses $u_{b,0}$ and $u_{b,-1}$ change due to the increased stiffness. However, the remaining mode shape and the corresponding frequency do not change with χ.

B. Analysis of the nonlinear interface

Based on the above observations, we seek to achieve a tunable response in our chain by using nonlinear springs whose stiffness depends on the amplitude. An effect similar to the frequency shift due to springs with stiffness χk_1 in the above linear chain may be obtained by varying the excitation force amplitude. We consider a chain identical to the above linear chain with an interface, but we replace the two interface springs having stiffness χk_1 with weakly nonlinear springs, whose restoring force varies with relative displacement Δu as $F = k_1 \Delta u + \Gamma(\Delta u)^3$. Adding a cubic nonlinearity leads to an amplitude-dependent frequency of the interface mode. Viscous damping with coefficient c is applied to the mass at the interface so that a steady-state can be reached in our numerical simulations. We show how the nonlinear chain behaves essentially as a Duffing oscillator using a reduced order model for the interface mass, similar to Eq. (6). Our analytical results thus provide the opportunity to apply known results on Duffing oscillators to the investigation of edge modes in nonlinear regimes.

We investigate the forced vibration response of this nonlinear chain subjected to an external excitation force f applied at the interface mass. The governing equation for the mass at the interface and its adjacent masses may be written as

$$\begin{aligned} &m\ddot{u}_{c,0} + c\dot{u}_{c,0} + k_1(2u_{c,0} - u_{b,0} - u_{b,-1}) \\ &\quad + \Gamma(u_{c,0} - u_{b,0})^3 + \Gamma(u_{c,0} - u_{b,-1})^3 = f\cos(\Omega t), \\ &m\ddot{u}_{b,0} + k_1(u_{b,0} - u_{c,0}) + k_2(u_{b,0} - u_{a,1}) \\ &\quad + \Gamma(u_{b,0} - u_{c,0})^3 = 0, \\ &m\ddot{u}_{b,-1} + k_1(u_{b,-1} - u_{c,0}) + k_2(u_{b,-1} - u_{a,-1}) \\ &\quad + \Gamma(u_{b,-1} - u_{c,0})^3 = 0. \end{aligned} \tag{7}$$

The governing equations for all the other masses on both sides of the interface remain the same as in the linear case [Eqs. (2) and (3)]. Again, we consider a chain with stiffness parameter $\gamma < 0$, and we derive the equivalent behavior of the interface mass in the band-gap frequencies.

To now get an equivalent equation for the interface mass, we need to eliminate $u_{b,0}$ from the governing equation of the interface mass. Let us assume an approximate solution for the displacement of the masses in the chain to be of the form

$$\boldsymbol{u} = \frac{\boldsymbol{v}e^{i\Omega t}}{2} + \epsilon \sum_{n=2}^{M} (\boldsymbol{w}_n e^{in\Omega\tau}) + \text{c.c.}, \tag{8}$$

with ϵ being a bookkeeping parameter and c.c. denoting the complex conjugate. Recall that e_1 and e_2 are the components of the eigenvector corresponding to the localized mode in the linear chain [Eq. (A9)]. The nonlinear force term may be approximated as

$$\Gamma(u_{c,0} - u_{b,0})^3 = \frac{3}{8}\Gamma\left(1 - \frac{e_2}{e_1}\right)^3 |v_{c,0}|^2 v_{c,0} e^{i\Omega t} + \epsilon(\text{h.h.}), \tag{9}$$

where h.h. denotes higher harmonics. Note that the above approximation is valid for small displacements when the term $u_{b,0}/u_{c,0}$ can be approximated by the linear solution ($\boldsymbol{u}_0 = s\boldsymbol{e}$).

We perform a harmonic balance on the linear parts of the chain by considering only the terms of frequency Ω. The displacements in the linear parts of the chain can be related using the transfer-matrix approach. Observe that the structure of the chain results in exactly the same relation as Eq. (A2) holding between $(v_{b,p-1}, v_{a,p})$ and $(v_{b,p}, v_{a,p+1})$ under the transformation $\gamma \to -\gamma$. Thus, defining the corresponding quantities $\overline{\boldsymbol{S}}(\gamma) = \boldsymbol{S}(-\gamma) = \boldsymbol{T}^{-N}(-\gamma)$ leads to the following relation:

$$\overline{S}_{12} v_{b,0} - \overline{S}_{11} v_{a,1} = 0. \tag{10}$$

Imposing Eq. (8) and again performing a harmonic balance, the equation for the displacement $v_{b,0}$ of the mass adjacent to the interface mass now becomes

$$-\Omega^2 v_{b,0} + (1+\gamma)(v_{b,0} - v_{c,0}) + (1-\gamma)(v_{b,0} - v_{a,1}) - \frac{3\Gamma}{4}\left(1 - \frac{e_2}{e_1}\right)^3 |v_{c,0}|^2 v_{c,0} = 0.$$

Eliminating $v_{a,1}$ from the above equation using Eq. (10), it may be rewritten as

$$\left[2 - \Omega^2 - (1-\gamma)\frac{\overline{S}_{12}}{\overline{S}_{11}}\right] v_{b,0} = \frac{3\Gamma}{4}\left(1 - \frac{e_2}{e_1}\right)^3 |v_{c,0}|^2 v_{c,0} + (1+\gamma) v_{c,0}. \quad (11)$$

We may write an equation similar to Eq. (11) for the displacement $u_{b,-1}$ of the mass at the left of the interface mass and use an approximation similar to Eq. (9) to simplify its cubic nonlinear term. Indeed, for the case $\gamma < 0$, recall that the zeroth-order solution is an antisymmetric mode and thus $v_{b,0} = v_{b,-1}$. Substituting Eq. (11) and its counterpart for $u_{b,-1}$ into the governing equation for the interface mass and performing a harmonic balance again leads to the following equation:

$$-\Omega^2 v_{c,0} + i\Omega\delta v_{c,0} + (1+\gamma)\left(2 - \frac{1+\gamma}{g}\right) v_{c,0} + \frac{3\Gamma}{4}\left(1 - \frac{1+\gamma}{g}\right)\left(1 - \frac{e_2}{e_1}\right)^3 |v_{c,0}|^2 v_{c,0} = f, \quad (12)$$

where $g = 2 - \Omega^2 - (1-\gamma)\overline{S}_{12}/\overline{S}_{11}$, and $\delta = c\sqrt{2/km}$ is the nondimensional damping parameter. Decomposing $v_{0,c} = v_R + i v_I$ into its real and imaginary parts leads to two equations. Squaring and summing them leads to the following frequency amplitude response [38]:

$$\left[\left(\Omega^2 - k_e - \frac{3}{4}\Gamma_e u^2\right)^2 + (\delta\Omega)^2\right] u^2 = f^2, \quad (13)$$

with $u = |v_{0,c}|$ being the displacement amplitude and

$$k_e = (1+\gamma)\left(2 - \frac{1+\gamma}{g}\right),$$

$$\Gamma_e = \Gamma\left(1 - \frac{1+\gamma}{g}\right)\left(1 - \frac{e_2}{e_1}\right)^3.$$

The above frequency amplitude response is similar to that of a Duffing oscillator with linear stiffness k_e and nonlinear force Γ_e excited near the resonant frequency [38].

Let us first consider a chain with strain-hardening springs ($\Gamma > 0$) connected to the interface mass. The dynamic response of the chain is investigated using the amplitude-response predicted by the reduced order model [Eq. (13)] and transient simulations of the full nonlinear chain, performed using the Verlet algorithm [39]. We compare the frequency response function predicted by the reduced order model with numerical simulations on a finite chain. The numerical simulations are performed until the chain attains a steady state. The damping coefficient and the linear and nonlinear stiffness parameter values are set to $\delta = 0.01$, $\gamma = 0.4$, and $\Gamma = 0.1$, respectively. The interface mass is subjected to an external force $f\cos(\Omega\tau)$. The frequency response is computed by normalizing the displacement $u_{c,0}$ of the interface mass by the excitation force amplitude f as $A_I = u_{c,0}k/f$.

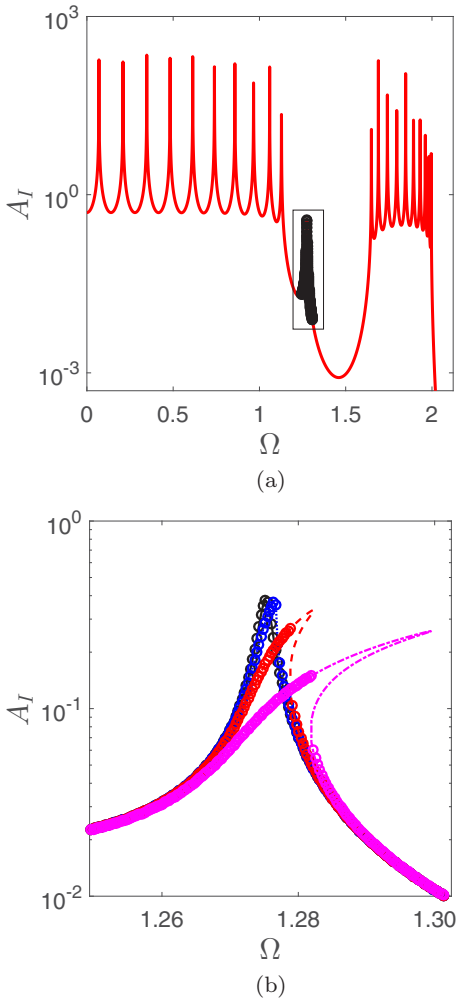

FIG. 4. Frequency response of the interface mass normalized by excitation force f. (a) Both the finite chain numerical simulations (red curve) and the analytical solution of the reduced model (black circles) show an interface mode for small forcing amplitude $f = 1$. (b) Numerical (markers) and analytical (curves) solutions for various force amplitudes $f = \{1,4,10,25\}$. Curves shift to the right and the chain behaves as a Duffing oscillator for frequencies near the interface mode.

Figure 4(a) displays the frequency response of a finite linear chain (red curve) over $\Omega \in [0, 2]$ along with the response observed from simulations of the finite nonlinear chain (black circles) for frequencies in the vicinity of the interface mode frequency when subjected to low-amplitude excitation ($f_0 = 1$). The linear chain response is obtained by solving the forced vibration response at steady state using Eq. (5). Since the excitation force amplitude is low, nonlinear effects are seen to be negligible, and the predictions of the linear model are in good agreement with the numerical simulations for frequencies near the interface mode frequency.

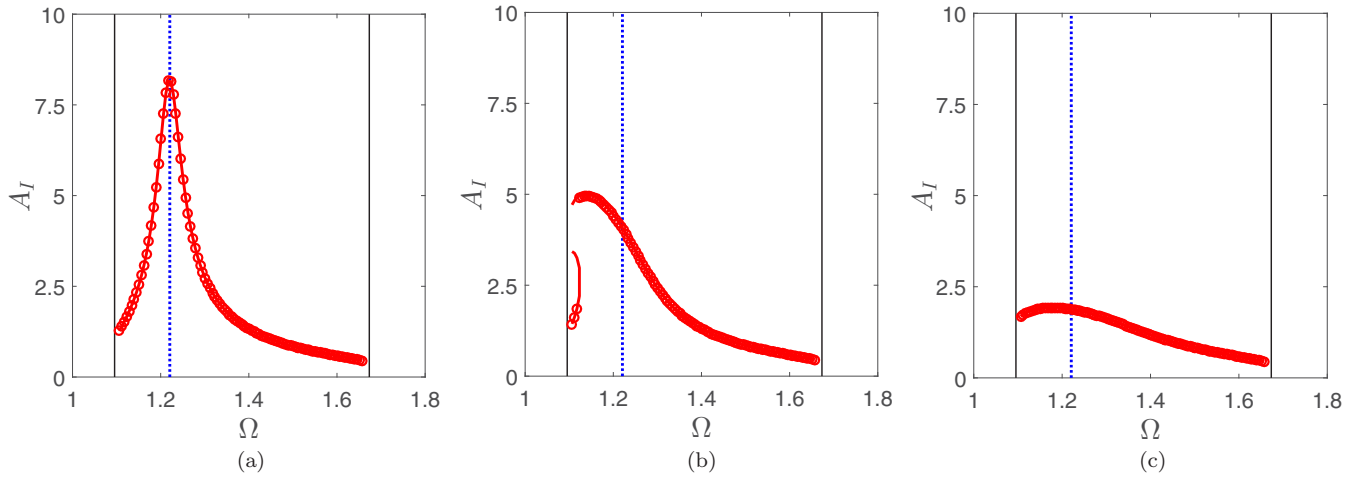

FIG. 5. Analytical (curve) and numerical (circles) responses of a nonlinear chain excited at the interface with force amplitude f. The responses for various excitation amplitudes (a) $f = 0.001$, (b) $f = 0.06$, and (c) $f = 0.2$ are normalized by f and are distinct due to nonlinearity.

Figure 4(b) displays a closeup view of the frequency response computed from simulations of the finite nonlinear chain (markers), along with the response given by Eq. (13), the nonlinear reduced order model (solid curves), for various force excitation amplitudes $f = \{1,4,10,25\}$. An excellent agreement is obtained between them, which confirms the validity of our reduced order model. The peak force shifts to the right with increasing force amplitude and displays a backbone curve. This behavior is typical of a Duffing oscillator [38] and demonstrates the amplitude-dependent behavior of the interface mode.

Let us now exploit the amplitude-dependent behavior to migrate the localized mode into the bulk bands. By varying the amplitude, the localized mode can be eliminated from the band-gap frequencies. The damping coefficient and the linear and nonlinear stiffness parameter values are set to $\delta = 0.01$, $\gamma = -0.4$, and $\Gamma = -1$, respectively. Notice that strain-softening springs ($\Gamma < 0$) are used for this purpose. The interface mass in the chain is subjected to the same excitation as in the previous strain-hardening case. Figure 5 displays the frequency response function for the displacement of the interface mass predicted by Eq. (13) for three levels of forcing amplitude: (a) $f = 0.006$, (b) $f = 0.06$, and (c) $f = 0.2$. The solid vertical lines depict the frequency bounds of the band gaps, while the dashed (blue) vertical line shows the frequency of the interface mode when the chain is linear ($\Gamma = 0$). The markers denote the numerical solution obtained by solving the transient problem of an equivalent single degree of freedom Duffing oscillator until steady state (with stiffness parameters k_e and Γ_e), while the solid curves denote the frequency amplitude response of Eq. (13). The interface mode frequency and the normalized amplitude both decrease with increasing force amplitude, which is consistent with the behavior of a Duffing oscillator. As the amplitude increases, the frequency associated with the interface mode moves into the bulk bands from the band gaps.

Having demonstrated how to shift the localized mode frequency into the bulk bands using a reduced single degree of freedom model, let us finally show how this shifting leads to a reduction in the response of a finite chain. We consider a chain of 20 unit cells with an interface mass at the center and subject the mass at the left end to a harmonic displacement, while the mass at the right end is free. Figure 6 displays the normalized frequency response in the band-gap frequencies for two values of excitation force amplitude: $f = 0.001$ (solid curves) and $f = 0.06$ (dashed curves). Figure 6(a) displays a closeup of the frequency response near the interface mode frequency Ω_i. The frequency response is similar to the linear case, and nonlinear effects are negligible for small-amplitude excitations ($f \leqslant 0.001$), while moderate amplitudes ($f > 0.01$) lead to a reduction in the displacement amplitude by an order of magnitude. The interface mode frequency shifts toward the lower end of the band gap, decreasing the response at the interface. Thus the frequency-shifting behavior is demonstrated by first showing its analogy with a Duffing oscillator using our reduced model and then verifying these predictions with numerical simulations on a finite chain. In summary, amplitude-dependent behavior and multiple stable solutions are observed for chains with stiffness parameter $\gamma < 0$. This behavior is predicted analytically by showing the equivalence of the edge mode with a Duffing oscillator. Furthermore, the edge mode frequency is independent of the wave amplitude for $\gamma > 0$. This unexpected observation is explained by examining the analytical solution of eigenmodes associated with this edge mode.

III. TUNABLE EDGE MODES IN 2D LATTICES

We now extend the ideas presented in the previous section to 2D lattices. We consider the 2D lattice in Pal *et al.* [13], which implements a mechanical analog of the quantum spin Hall effect and supports topologically protected edge modes. An amplitude-dependent response is obtained by using weakly nonlinear springs. We present a dispersion analysis of a unit cell and of an extended unit cell computed using an asymptotic analysis. In contrast to the interface mode in the 1D lattice, we show the ability of the considered lattice to undergo transitions from bulk-to-edge mode-dominated by varying the excitation amplitude both for hardening and softening springs. Finally, we present numerical simulations on finite lattices to illustrate the amplitude-dependent nature of wave propagation due to nonlinearities.

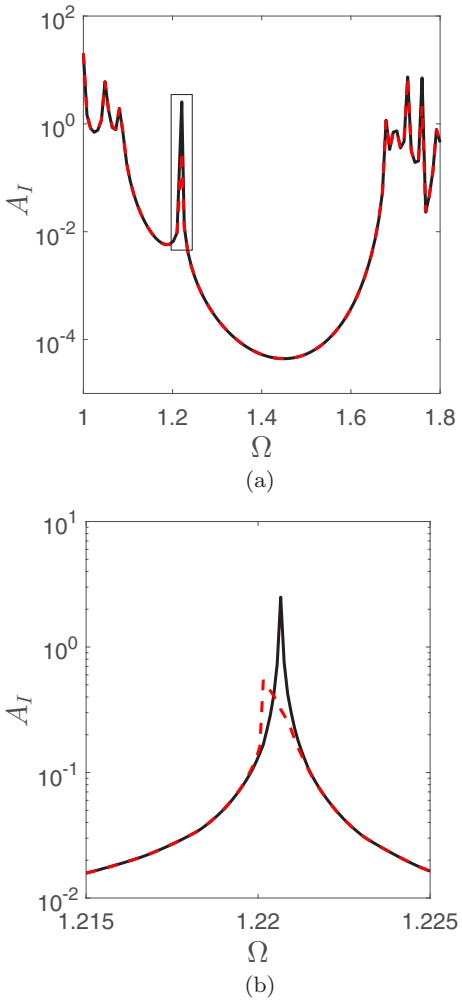

FIG. 6. Transient response of a nonlinear chain with $\Gamma < 0$ excited at one end. The normalized amplitude response in the band gaps at high excitation amplitudes (dashed red line, $f = 0.06$) is an order of magnitude lower than at low amplitudes (solid black line, $f = 0.001$).

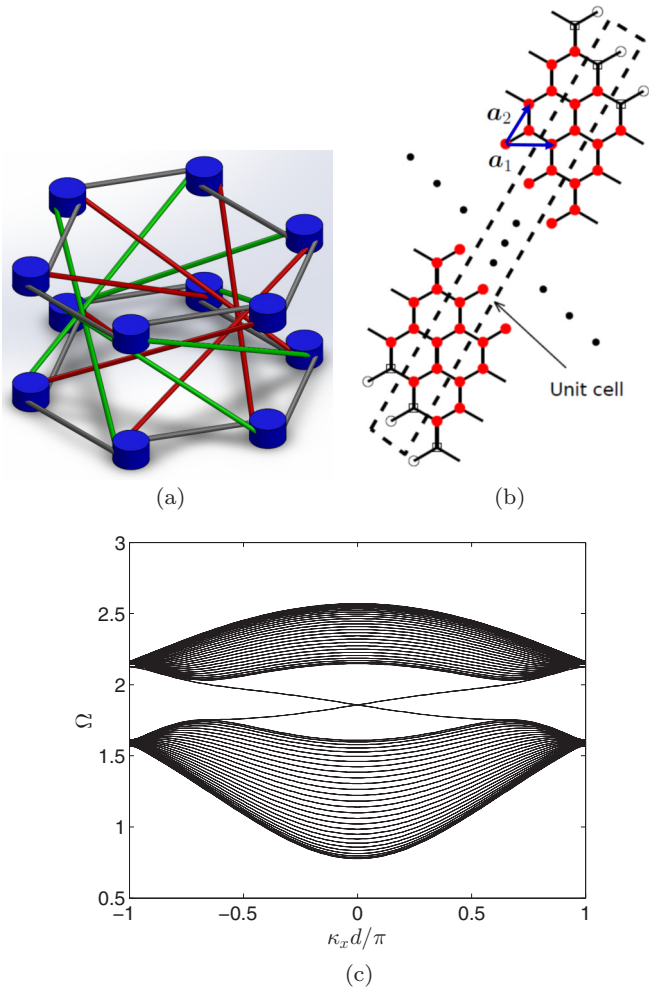

FIG. 7. (a) A hexagonal cell of the lattice, having two layers with normal in-plane springs and a combination of normal and reverse springs between the two layers. (b) Finite strip with fixed boundaries. The nodes with filled (red) circles are free, while the others are fixed. (c) Dispersion diagram of the finite strip showing edge modes spanning the two sets of bulk modes.

A. Lattice configuration

The lattice consists of two layers of a hexagonal lattice spanning the xy plane, and its lattice vectors are $\boldsymbol{a}_1 = (-1/2, \sqrt{3}/2)$ and $\boldsymbol{a}_2 = (1/2, \sqrt{3}/2)$. Figure 7(a) displays a schematic of a single hexagonal cell. Each node is a disk that rotates about the z axis, perpendicular to the plane of the lattice. Two kinds of springs—normal and chiral—connect the disks. The in-plane springs [gray color in Fig. 7(a)] are linear and they provide a torque $k(\theta_j - \theta_i)$ on disk i due to rotations θ_i and θ_j of the two nearest-neighbor disks connected to the spring. A combination of normal [n, green color in Fig. 7(a)] and chiral [ch, red color in Fig. 7(a)] springs connect the second nearest neighbors on adjacent layers in our lattice. These springs are weakly nonlinear, and the torque-rotation relations between two disks i, j are, respectively,

$$T_i^n = k_n(\theta_j - \theta_i) + \epsilon_n(\theta_j - \theta_i)^3, \tag{14a}$$

$$T_i^{\mathrm{ch}} = -k_{\mathrm{ch}}(\theta_j + \theta_i) - \epsilon_{\mathrm{ch}}(\theta_j + \theta_i)^3. \tag{14b}$$

B. Dispersion analysis of linear and nonlinear lattices

Dispersion studies are conducted both for a single hexagonal unit cell having four degrees of freedom (two in each layer) and for a unit cell of a strip that is periodic along one direction, as illustrated in Fig. 7(b). Let us set $\boldsymbol{u}$ as the vector whose components are the generalized displacement for all the degrees of freedom in a unit cell, which in our case would be the rotation of disks at each lattice site. In [13], the authors show that this lattice has a band gap for bulk modes. Furthermore, there are topologically protected edge modes in this band gap that propagate along the boundaries of the lattice. We seek to investigate how weak nonlinearities affect the edge modes in our lattice. To get the dispersion relation of a nonlinear lattice, we use a perturbation-based method to seek corrections to the linear dispersion relation $\omega = \omega(\boldsymbol{\mu})$, with $\boldsymbol{\mu}$ being the two-dimensional wave vector. Based on the method of multiple scales, the following asymptotic expansion for the displacement components in a unit cell and frequency

is imposed:

$$\boldsymbol{u} = \boldsymbol{u}_0 + \epsilon \boldsymbol{u}_1 + O(\epsilon^2),$$
$$\omega = \omega_0 + \epsilon \omega_1 + O(\epsilon^2).$$

The asymptotic procedure we follow is similar to that of Leamy and co-workers [35,36], and its details are presented in Appendix D.

We first present the dispersion behavior of a finite strip of a linear lattice to illustrate the existence of localized edge modes. Then, two kinds of nonlinear springs, namely strain hardening and strain softening, are considered to demonstrate the amplitude-dependent nature of these edge modes. The equations are normalized using the time scale $\sqrt{k/I}$, with I being the rotational inertia of the disks. In nondimensional form (with superscript $\tilde{k}$), both the normal and chiral springs connecting adjacent layers are chosen to have a linear stiffness component $\tilde{k}_n = \tilde{k}_{\text{ch}} = 0.1$, and their nonlinear components are equal ($\epsilon = \tilde{\epsilon}_n = \tilde{\epsilon}_{\text{ch}}$).

1. Dispersion analysis of a strip

To illustrate the presence of edge modes in our lattice, let us consider a finite strip of 20 unit cells as illustrated in Fig. 7(b). The strip is periodic in the $\boldsymbol{a}_1$ direction and has a finite width in the $\boldsymbol{a}_2$ direction. The nodes with red (filled circle) markers are free to move, while the nodes with unfilled circles and squares at either boundary are fixed nodes. A dispersion analysis is conducted on this finite strip, which is periodic in the $\boldsymbol{a}_1$ direction, and the dashed rectangle shows the unit cell. By imposing a traveling-wave solution of the form $\boldsymbol{u} = \boldsymbol{u}(\kappa_x)e^{i(\Omega t - \kappa_x x)}$ on the lattice, an eigenvalue problem is obtained for each wave number κ_x. Note that the x axis is oriented along the $\boldsymbol{a}_1$ direction.

Figure 7(c) displays the dispersion diagram for the finite strip under study. The wave number κ_1 is projected onto the x axis. There are two sets of wave modes: the first set spans [0.78, 1.75] and the second set spans [2.03, 2.55]. These two sets correspond to bulk modes, and the two modes between them are edge modes. The eigenvectors corresponding to these frequencies are localized at the edges. We remark here on the choice of boundary conditions as shown in Fig. 7(b). Note that allowing the nodes with square markers to be free results in a different type of edge mode than the one illustrated in Fig. 7(b). The work in [13] presented the band diagrams when the nodes having square markers were not fixed. There are two overlapping bands at each point in the dispersion diagrams in Fig. 7(c). The lattice supports two traveling waves at the edge of the lattice: one in the clockwise and the other in the counterclockwise direction. Furthermore, these modes are topologically protected: they span the entire band gaps and they cannot be localized by small disorders or perturbations [40].

2. Strain hardening springs

Having demonstrated the presence of edge modes in a linear lattice, we now investigate the effect of introducing nonlinear interactions between the interlayer springs. Figure 8 displays the dispersion diagram when the nonlinearity is of the strain-hardening type ($\epsilon = 0.05$) with amplitude of the waves $A_0 = 0.6$. The first-order correction is computed using an asymptotic analysis [Eq. (D8) in Appendix D] at each two-dimensional wave vector $\boldsymbol{\mu}$ for both a unit cell in the bulk and a unit cell comprised of a finite strip. Figure 8(a) displays the bulk dispersion surface projected onto the x axis along with the edge modes computed from the finite strip. A comparison with the dispersion diagram of the finite strip in the linear case shows that the lower band remains unchanged while the lower surface of the upper band shifts upward.

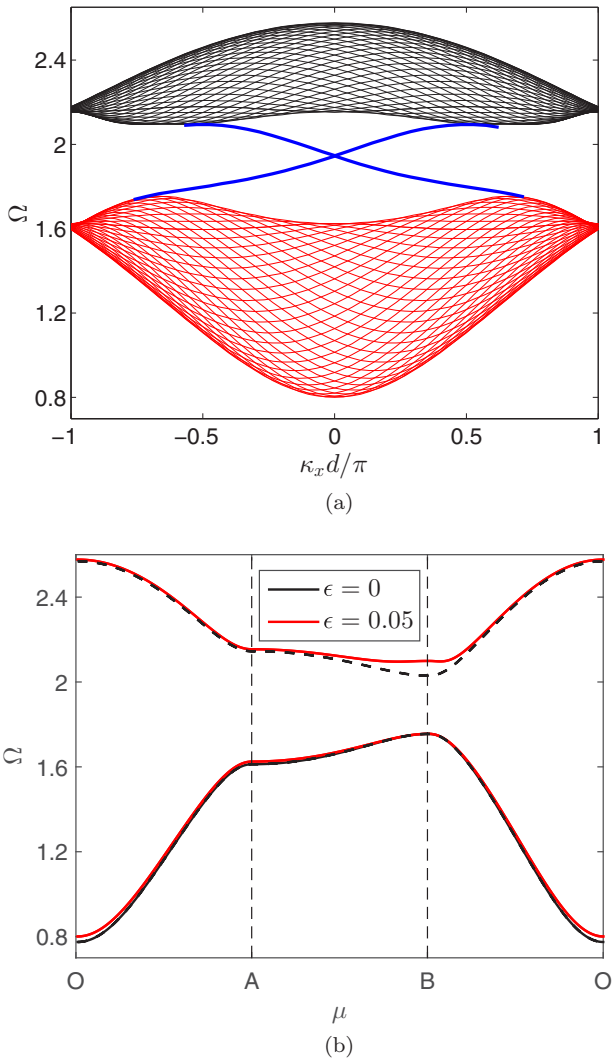

FIG. 8. Dispersion diagram for both linear ($\epsilon = 0$) and strain-hardening springs $\epsilon = 0.05$ over (a) a strip and (b) the irreducible Brillouin zone. The edge modes traverse the band gaps and the optical band shifts upward near point B in the nonlinear lattice.

Figure 8(b) displays the dispersion curves along the boundary of the irreducible Brillouin zone for both the linear (dashed curves) and nonlinear (solid curves) lattices. Since the hexagonal lattice has a sixfold symmetry, the IBZ is a triangle and we choose it to span the points $O : (0,0)$, $A : (0,\pi)$, and $B : (2\pi/3, 2\pi/3)$ in the reciprocal-lattice space. The presence of interplanar springs leads to a band gap for bulk waves, as shown in Fig. 8(b), and the existence of edge waves in this band gap. We see that the lower band does not get significantly affected due to the nonlinear springs. However, the upper band

in the vicinity of point B gets shifted upward and the band gap widens as a consequence. Note that the edge modes continue to span the band gaps, and they do not localize (group velocity is nonzero) in the presence of nonlinear interactions.

We now elaborate how the above observations can be exploited to achieve amplitude-dependent edge waves using our nonlinear lattices. At small amplitudes, the dynamic response is similar to a lattice with no nonlinear springs, and it corresponds to the $\epsilon = 0$ case in Fig. 8. However, as the amplitude increases, nonlinear effects come into play and the behavior resembles the nonlinear case, illustrated by $\epsilon = 0.05$ in Fig. 8. Thus exciting at a frequency at the tip of the lower surface of the Brillouin zone near point B will result in amplitude-dependent edge waves. At small amplitudes there will be no edge waves, while at high amplitudes the band widens and one-way edge waves propagate in the lattice.

3. Strain-softening springs

We now turn attention to the study of nonlinear springs of the strain-softening type having $\epsilon < 0$. A similar dispersion analysis is conducted on both a strip and a single unit cell with nonlinear stiffness parameter $\epsilon = -0.5$ and wave amplitude $A_0 = 0.6$. Figure 9(a) displays the dispersion surface of both the bulk and edge modes projected onto the x axis. Similar to the earlier case with $\epsilon > 0$, the lower band does not change significantly due to the nonlinear springs. The lower surface of the upper band shifts downward, which is consistent with the behavior for the $\epsilon > 0$ case, since the first-order correction $\epsilon\omega_1$ is linearly proportional to ϵ. Figure 9(b) displays the dispersion curves along the boundary of the IBZ. In contrast with the strain-hardening case, here the dispersion curves shift downward near point B while remaining relatively unaltered away from this point. Similar to the strain-hardening case, these softening springs can be exploited to get an amplitude-dependent response of the lattice. The lattice behavior can be changed from edge waves at low amplitudes to bulk waves at high amplitudes. We thus illustrated the amplitude-dependent nature of the dispersion curves for the strain-softening nonlinear springs.

C. Numerical simulations of wave propagation

We now conduct numerical simulations to demonstrate the effect of nonlinear interactions on wave propagation in a finite lattice. The numerical results are interpreted using the dispersion diagrams for linear and nonlinear lattices that were presented earlier in Sec. III B. All our numerical simulations are conducted on a lattice of 30×30 unit cells using a fourth-order Runge-Kutta explicit time integration scheme. The boundary nodes of our lattice are fixed similar to that illustrated in Fig. 7(b). The lattice is subjected to a point excitation at a specific frequency on a boundary node lying at the center of the lower left boundary. Two examples are presented: the first one demonstrates edge wave propagation at high amplitudes, while the second example demonstrates the decaying of edge waves with increasing amplitude.

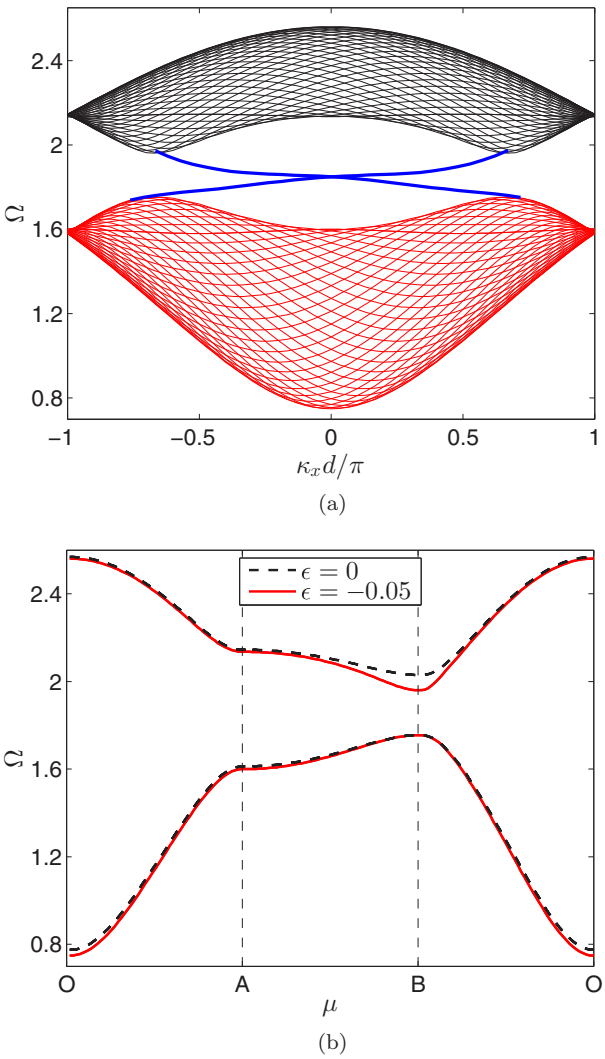

FIG. 9. Dispersion diagram for lattices with linear ($\epsilon = 0$) and strain-softening springs $\epsilon = -0.05$ over (a) a strip and (b) the irreducible Brillouin zone. The edge modes traverse the band gaps and the optical band shifts downward near point B in the nonlinear lattice.

1. High-amplitude edge waves

In this example, the lattice is comprised of nonlinear springs of the strain-hardening type with $\epsilon = 0.05$. Two numerical simulations are conducted: one at low ($A = 6 \times 10^{-3}$) and the other at high ($A = 6 \times 10^{-1}$) force excitation amplitudes. A boundary lattice site is subjected to a harmonic excitation at frequency $\Omega = 2.045$. The dispersion analysis in Fig. 8 shows that this frequency lies in the lower part of the top band and the linear lattice supports bulk waves and no edge waves. As discussed earlier in Sec. III B 2, at higher amplitudes, the band gap widens and edge modes exist at higher frequencies. The top and bottom layers are subject to the excitation

$$F_{\text{top}} = A\cos\omega t, \quad F_{\text{bottom}} = A\sin\omega t. \tag{15}$$

Figure 10 displays the angular displacement of the disks at the various nodes. The color scale ranges for the two cases are $[0, 8 \times 10^{-3}]$ and $[0, 8 \times 10^{-1}]$. The colors show the magnitude (l_2 norm) of the displacement vector at each

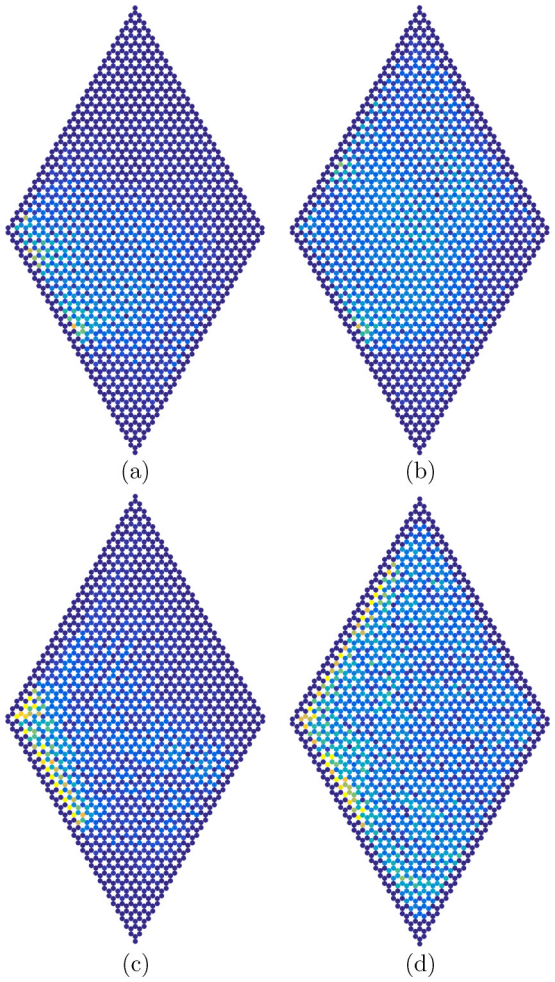

FIG. 10. Displacement magnitude at each lattice site at two time instants ($\tau = 200,400$) for a lattice with $\epsilon = 0.05$ subjected to two force amplitudes (a,b) $A = 6 \times 10^{-3}$, (c,d) $A = 6 \times 10^{-1}$, and excitation frequency $\Omega = 2.045$. The lattice supports bulk and edge waves at low and high amplitudes, respectively.

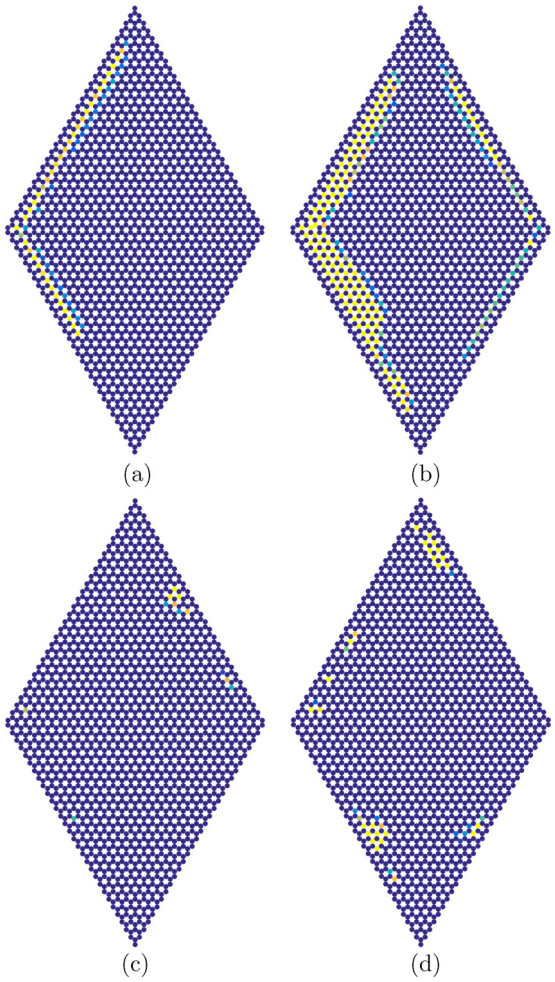

FIG. 11. Displacement magnitude at each lattice site at two time instants ($\tau = 400,1000$) for a lattice with $\epsilon = 0.05$ subjected to two force amplitudes (a,b) $A = 2 \times 10^{-3}$, (c,d) $A = 2 \times 10^{-1}$, and excitation frequency $\Omega = 2.02$. The lattice supports edge waves at low amplitudes and bulk waves at high amplitudes. The color scale has a range (a,b) $[2.4 \times 10^{-3}, 3 \times 10^{-3}]$ and (c,d) $[2.4 \times 10^{-1}, 3 \times 10^{-1}]$.

lattice site. Note that there are two disks (one at the top and one at the bottom layer) at each lattice site, and the displacement vector thus has two components denoting the angular displacement of these two disks. Figures 10(a) and 10(b) display the displacement magnitude for the low-amplitude excitation at times $\tau = 200$ and 400. It is observed that the wave propagation is isotropic from the point of excitation into the lattice, and this behavior is consistent with the predictions of the dispersion analysis as there are no edge waves at the excitation frequency. Figures 10(c) and 10(d) displays the displacement magnitude for high-amplitude excitation at the same time instants. Edge waves are observed to propagate in the counterclockwise direction, which is indeed consistent with the behavior predicted in the dispersion analysis in Sec. III B 2.

2. Bulk waves at high amplitudes

Our next example involves strain-softening springs having $\epsilon < 0$. Again, the lattice is subjected to a point excitation at a frequency $\Omega = 2.02$ with the top and bottom disks at the node having a phase difference of $\pi/2$ as in Eq. (15). At this frequency, there are no bulk modes in the linear lattice, and edge waves traverse through the lattice. As discussed in Sec. III B 3, nonlinear interactions lead to shortening of the band gap, and edge modes do not propagate at high amplitudes.

Figures 11(a) and 11(b) display the displacement magnitude in the lattice for the low-amplitude excitation case with $A = 2 \times 10^{-3}$ at two time instants $\tau = 400$ and 1000. The color scale has a maximum value 3×10^{-3} and a minimum value 1.6×10^{-3}. We observe edge waves propagating through the lattice in the clockwise direction. Figures 11(c) and 11(d) display the magnitude of the displacement vector at each lattice site for the high-amplitude force excitation case with $A = 2.0 \times 10^{-1}$ at the same time instants. The color scale has a maximum value 3×10^{-1}. It is observed that energy propagates into the lattice, and the amount of energy concentrated on the edge is lower than in the low-amplitude case. However, note that the waves propagate into the interior only until the amplitude of the edge wave is higher than the threshold required to have bulk modes. Note that as the amplitude

keeps decreasing, it will reach a value where edge modes are supported. Edge waves at or below this threshold keep propagating, and the lattice could be seen as a low-amplitude pass filter for edge waves at this particular excitation frequency. Thus we observe that, in contrast to the low-amplitude case, there is no wave propagation along the boundary. There are compact zones of energy localization where the displacement is high. These zones are attributed to energy localization as a consequence of multiple reflections of bulk waves. Indeed, as the dynamics evolves, these localized zones arise at different parts of the lattice boundary. Note that these are not compactly supported solitons that traverse a boundary. In conclusion, introducing nonlinearity provides a means to achieve tunability by varying the wave amplitude. Thus for a given frequency, we illustrated binary behavior: edge waves at one amplitude and bulk waves at another amplitude, by careful design of the lattice properties and loading conditions.

IV. CONCLUSIONS

This work illustrates how localized modes can be induced at the interface or boundaries of both one- and two-dimensional lattices. In the one-dimensional case, we consider a lattice of point masses connected by alternating springs. We showed that a mode exists in the band-gap frequencies and it is localized at the interface between two lattices that are inverted copies of each other. We derive explicit expressions for the frequencies of the localized modes for various interface types and their associated mode shapes. This localized interface mode can be made tunable by using weakly nonlinear springs at the interface of the two masses. We showed that the behavior of the interface mass is equivalent to a Duffing oscillator in the vicinity of this interface mode frequency, and we demonstrated how varying the force amplitude can lead to a frequency shift of the interface mode. By choosing the parameters carefully, one can control the existence of interface modes and move them from the band gap to the bulk bands by varying the force excitation amplitude.

In the second part, we investigate tunability using weakly nonlinear springs in a lattice that supports edge waves. We show how the dynamic response of the lattice can be varied from bulk to edge waves at a fixed frequency by varying the excitation amplitude. We use an asymptotic analysis to derive dispersion relations for both strain-hardening and strain-softening springs, and we demonstrate that the optical band can be shifted upward or downward. Finally, numerical simulations are presented to exemplify the theoretical predictions and illustrate the tunable nature of our lattices. This work illustrates how exploiting nonlinearities can lead to tunable lattices and mechanical structures supporting localized modes at interfaces and boundaries, and it opens the door for future research in tunable engineering structures and devices.

ACKNOWLEDGMENTS

The authors are indebted to the U.S. Army Research Office (Grant No. W911NF1210460), the U.S. Air Force Office of Scientific Research (Grant No. FA9550-13-1-0122), and the National Science Foundation (Grant No. 1332862) for financial support.

APPENDIX A: INTERFACE MODES

We seek the frequencies for which the above linear chain admits a localized mode solution at the interface, and we derive explicit expressions for their corresponding mode shapes. Let us consider a finite lattice having N unit cells on either side of the interface, with N large enough such that boundary effects are negligible in the dynamics of the interface mass. The unit cells are indexed from $p = -N$ to N so that the interface mass lies in the unit cell $p = 0$. To investigate the dynamics of this lattice in the band-gap frequencies, we impose a solution of the form $\boldsymbol{u}_p(t) = \boldsymbol{u}_p e^{i\Omega\tau}$ for all the lattice sites, where p denotes the cell index. A similar solution is also imposed on the interface mass. To relate the displacements in two neighboring cells $p-1$ and p on the right of the interface ($p > 0$), we rewrite the governing equations for the masses at the lattice sites b_{p-1} and a_p as

$$(2-\Omega^2)u_{a,p} - (1+\gamma)u_{b,p} - (1-\gamma)u_{b,p-1} = 0, \tag{A1a}$$

$$(2-\Omega^2)u_{b,p-1} - (1-\gamma)u_{a,p} - (1+\gamma)u_{a,p-1} = 0. \tag{A1b}$$

Rearranging the terms in the above equation yields a relation between the displacements of adjacent unit cells on the right side of the interface. In nondimensional form, this relation is expressed using a transfer matrix $\boldsymbol{T}$ as

$$\begin{pmatrix} u_a \\ u_b \end{pmatrix}_p = \begin{pmatrix} \frac{\gamma+1}{\gamma-1} & \frac{2-\Omega^2}{1-\gamma} \\ -\frac{2-\Omega^2}{1-\gamma} & \frac{(2-\Omega^2)^2-(\gamma-1)^2}{1-\gamma^2} \end{pmatrix} \begin{pmatrix} u_a \\ u_b \end{pmatrix}_{p-1} = \boldsymbol{T} \begin{pmatrix} u_a \\ u_b \end{pmatrix}_{p-1}. \tag{A2}$$

Using the above relation, the displacement at unit cell $p = N$ may be written in terms of the displacement at the interface unit cell ($p = 0$) as $\boldsymbol{u}_N = \boldsymbol{T}^N \boldsymbol{u}_0$. Note that the vector $\boldsymbol{u}_0$ has components $\boldsymbol{u}_0 = (u_{c,0},\, u_{b,0})^T$.

We now solve for the frequencies and corresponding mode shapes at which this chain has localized modes. We seek solutions that are localized at the interface and decay away from it, i.e., $\|\boldsymbol{u}_N\| \to 0$ as N becomes large. The solution procedure involves seeking eigensolutions of the transfer matrix $\boldsymbol{T}$ that satisfy the decay condition. For a mode localized at the interface, the displacement should decay away from the interface, i.e., $\|\boldsymbol{u}_N\| \to 0$ as $N \to \infty$. To make further progress, we use the following proposition: Let $\boldsymbol{T}$ be diagonalizable and let $(\lambda_i, \boldsymbol{e}_i)$ be its eigenvalue-vector pairs. Then, $\|\boldsymbol{T}^N \boldsymbol{u}\| \to 0$ as $N \to \infty$ with a nontrivial solution $\boldsymbol{u} \neq \boldsymbol{0}$ if and only if $\boldsymbol{u}$ is in the subspace spanned by the eigenvectors $\boldsymbol{e}_i$ whose corresponding eigenvalues satisfy $|\lambda_i| < 1$. To prove this statement, let us denote by $\boldsymbol{f}_i$ the subset of eigenvectors of $\boldsymbol{T}$ with associated eigenvalues $|\lambda_i| < 1$, and by $\boldsymbol{g}_j$ the eigenvectors with $|\lambda_j| \geqslant 1$. If $u = \sum \alpha_i \boldsymbol{f}_i$, then $T^N u = \sum \alpha_i {\lambda_i}^N \boldsymbol{f}_i$ and hence its norm goes to zero as N increases. We prove the "only if" part by contradiction. Assume that $\boldsymbol{u}$ is not in the $\boldsymbol{f}_i$ subspace as required. We may write $\boldsymbol{u} = \sum_i \alpha_i \boldsymbol{f}_i + \sum_j \beta_j \boldsymbol{g}_j$. Then $\boldsymbol{T}^N \boldsymbol{u} = \sum_i \alpha_i {\lambda_i}^N \boldsymbol{f}_i + \sum_j \beta_j {\lambda_j}^N \boldsymbol{g}_j$. Since there is a

nonzero β_j by assumption, the norm of this vector does not converge to 0 as $N \to \infty$, which completes the proof.

Note that the product of the eigenvalues of the transfer matrix $\boldsymbol{T}$ is unity since $\det(\boldsymbol{T}) = 1$. In the band-gap frequencies, the eigenvalues of $\boldsymbol{T}$ are real and distinct, hence exactly one eigenvalue satisfies $|\lambda_i| < 1$. The eigenvector corresponding to this eigenvalue is

$$\boldsymbol{e} = \begin{pmatrix} 2(\Omega^2-2)^2(1+\gamma) \\ (\Omega^2-2)^2 + 4\gamma + \Omega\sqrt{(\Omega^2-4)[(\Omega^2-2)^2-4\gamma^2]} \end{pmatrix}. \tag{A3}$$

The proposition above implies that a localized mode arises if the displacement $\boldsymbol{u}$ is a scalar multiple by the eigenvector $\boldsymbol{e}$, i.e., $\boldsymbol{e} = s\boldsymbol{u}_0$, with s being a scaling factor and $\boldsymbol{u}_0 = (u_{c,0},\, u_{b,0})$ having the displacement components of the unit cell at the interface. Let us now derive an expression for $\boldsymbol{u}_0$ from the governing equation of the interface mass. It may be rewritten as

$$2\left(1 - \frac{\Omega^2}{2(1+\gamma)}\right)u_{c,0} = (u_{b,0} + u_{b,-1}). \tag{A4}$$

Since the localized mode is nonpropagating and the lattices on either side of the interface mass are identical, symmetry conditions lead to the following relation between the masses adjacent to the interface mass:

$$|u_{b,0}| = |u_{b,-1}|. \tag{A5}$$

The above condition may be rewritten as $u_{b,-1} = e^{2i\theta}u_{b,0}$. Substituting this into Eq. (A4), the displacement $\boldsymbol{u}_0$ may be written as

$$\boldsymbol{u}_0 = \begin{pmatrix} e^{i\theta}\cos\theta \\ 1 - \frac{\Omega^2}{2(1+\gamma)} \end{pmatrix}. \tag{A6}$$

Note that the chain has band gaps in the frequency ranges $\Omega \in [\sqrt{2(1-|\gamma|)}, \sqrt{2(1+|\gamma|)}]$ and $\Omega > 2$; see Appendix B for details. Hence, the argument of the square root in Eq. (A3) is positive when Ω is in the band-gap frequencies and the components of $\boldsymbol{e}$ are real. The condition $\boldsymbol{e} = c\boldsymbol{u}_0$ implies $\theta = n\pi/2, n \in \mathbb{Z}$ and $e^{i\theta}\cos\theta \in \{0,1\}$. Applying this condition $(e_1/u_{c,0} = e_2/u_{b,0} = c)$ to the two cases separately allows us to solve for the frequencies Ω_i of the localized modes. $\theta = \pi/2$ leads to $\Omega = \sqrt{2}$, while $\theta = 0$ leads to the following equation:

$$[\Omega^2 - 2(1+\gamma)][\Omega^2 - 2(1-\gamma)](\Omega^2 - 4) = 4\gamma^2\Omega^2. \tag{A7}$$

Note that $\theta = 0$ implies $u_{b,0} = u_{b,1}$. From the transfer-matrix expression, we note that the mode shape is indeed antisymmetric about the interface mass. In contrast, $\theta = \pi/2$ leads to $u_{b,0} = -u_{b,-1}$ and $u_{c,0} = 0$. In this case, the mode shape is symmetric about the interface mass. Equation (A7) leads to the following expressions for the frequencies that support localized solutions:

$$\begin{aligned} &\gamma < 0: \quad \Omega = \sqrt{3 - \sqrt{1+8\gamma^2}}, && \text{antisymmetric mode,} \\ &\gamma > 0: \quad \Omega = \sqrt{2}, && \text{symmetric mode,} \\ &\gamma > 0: \quad \Omega = \sqrt{3 + \sqrt{1+8\gamma^2}}, && \text{antisymmetric mode.} \end{aligned} \tag{A8}$$

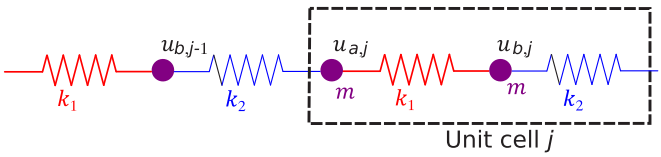

FIG. 12. Unit cell of an infinite spring mass chain having springs of alternating stiffness k_1 and k_2.

Substituting the frequencies Ω into the eigenvectors in Eq. (A3), taking appropriate signs under the square root, and checking the condition $\boldsymbol{e} = c\boldsymbol{u}_0$ show that the first solution is valid when $\gamma < 0$ and the other two solutions are valid when $\gamma > 0$. The displacement components of the interface unit cell for these localized modes are given by

$$\boldsymbol{e} = \begin{pmatrix} e_1 \\ e_2 \end{pmatrix} = \begin{pmatrix} u_{c,0} \\ u_{b,0} \end{pmatrix}, \tag{A9}$$

from which the displacement $\boldsymbol{u}_p$ of unit cell p can be obtained by using the relation $\boldsymbol{u}_p = \boldsymbol{T}^p\boldsymbol{u}_0$.

APPENDIX B: BAND INVERSION IN A LINEAR CHAIN

We consider a spring mass chain with springs of alternating stiffness k_1 and k_2 connecting identical masses as illustrated in Fig. 12. The unit cell is chosen as shown by the dashed box in Fig. 12. To normalize the governing equations, we express the spring stiffness as $k_1 = k(1+\gamma)$ and $k_2 = k(1-\gamma)$. Introducing the nondimensional time scale $\tau = t\sqrt{k/m}$, the governing equations for the masses in a unit cell may be expressed in nondimensional form as

$$\begin{aligned} &\ddot{u}_{a,j} + 2u_{a,j} - (1+\gamma)u_{b,j} - (1-\gamma)u_{b,j-1} = 0, \\ &\ddot{u}_{b,j} + 2u_{b,j} - (1+\gamma)u_{a,j} - (1-\gamma)u_{a,j+1} = 0. \end{aligned}$$

We first study the dynamic behavior of the lattice using a dispersion analysis. Imposing a plane-wave solution of the form $\boldsymbol{u}_j = (u_{a,j}, u_{b,j}) = \boldsymbol{A}(\mu)e^{i\Omega\tau + i\mu j}$, where Ω is the frequency and μ is the nondimensional wave number, leads to the following eigenvalue problem:

$$\begin{pmatrix} 2-\Omega^2 & -(1+\gamma) - (1-\gamma)e^{-i\mu} \\ -(1+\gamma) - (1-\gamma)e^{i\mu} & 2-\Omega^2 \end{pmatrix}\begin{pmatrix} A_a \\ A_b \end{pmatrix} = \Omega^2\begin{pmatrix} A_a \\ A_b \end{pmatrix}. \tag{B1}$$

The eigenvalues lead to two branches with frequencies $\Omega = \sqrt{2 \pm \sqrt{2+2\gamma^2+2(1-\gamma^2)\cos\mu}}$, with the minus and plus signs for the acoustic and optical bands, respectively. The lattice has a band gap over the frequency range $\Omega \in (\sqrt{2(1-|\gamma|)}, \sqrt{2(1+|\gamma|)})$.

Figure 13(a) displays the dispersion diagrams for stiffness parameters $\gamma = 0$ (green dotted curves) and $\gamma = 0.4$ (black solid curves). Figure 13(b) displays the frequencies bounding the band gap between the acoustic and optical branches as the stiffness parameter γ varies. Note that these bounding frequencies are at the wave number $\mu = \pi$. The frequency on the dashed (red) curve has an eigenvector $(A_a, A_b) = (1/\sqrt{2},\, 1/\sqrt{2})^T$ while that on the solid (blue) curve has

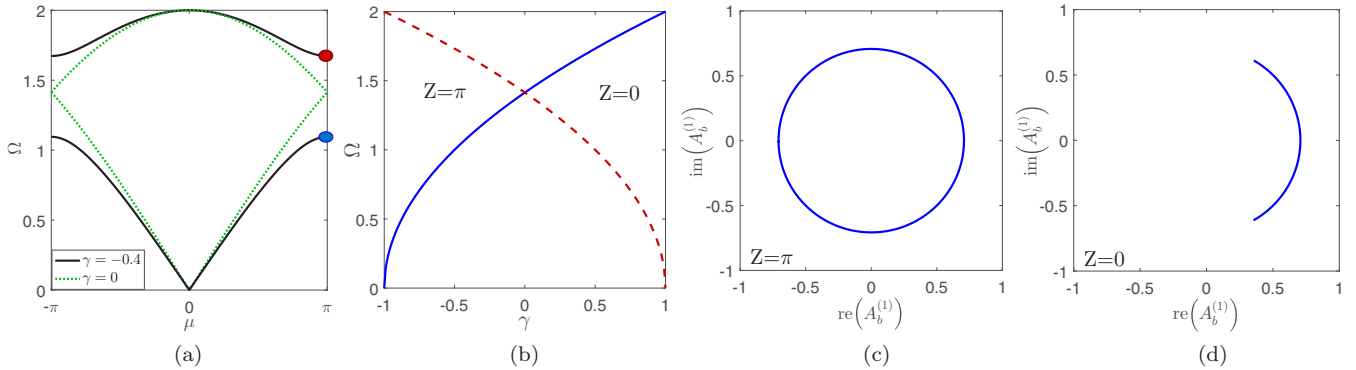

FIG. 13. (a) Dispersion relations for lattices with $\gamma = 0$ (dotted) and $\gamma = -0.5$ (solid). (b) Limits of the band gap showing band inversion as γ varies. Component 2 of eigenvector $A^{(1)}(\mu)$ as μ varies from $-\pi$ to π. (c) $\gamma = -0.5$ has a Zak phase π while (d) $\gamma = 0.5$ has a zero Zak phase.

an eigenvector $(1/\sqrt{2},\ -1/\sqrt{2})^T$ for all nonzero γ values. Note that the modes get inverted, i.e., the antisymmetric $(1/\sqrt{2}, -1/\sqrt{2})^T$ mode has a higher frequency than the symmetric $(1/\sqrt{2},\ 1/\sqrt{2})^T$ mode as γ increases beyond zero. This phenomenon is called band inversion and has been previously exploited in electronic systems [40–42] and continuous acoustic ones [19] to obtain localized modes. These modes are localized at the interface of two lattices: one with $\gamma > 0$ and the other with $\gamma < 0$.

To shed additional light on the topological properties of the eigensolutions, we examine the eigenvectors of lattices with $\gamma > 0$ and $\gamma < 0$. In particular, we study how they vary with wave number μ over the first Brillouin zone. Observe that the matrix in Eq. (B1) gives the same eigenvalues under the transformation $\gamma \to -\gamma$ but the eigenvectors are different. Indeed, note that the transformation $\gamma \to -\gamma$ may be achieved by simply reversing the direction of the lattice basis vector. An alternate way is to simply translate the unit cell by one mass to the right or left and relabel the masses appropriately. Both these changes correspond to changes in gauge and they change the eigenvectors, thereby changing the topology of the vector bundle associated with the solution of the above eigenvalue problem. We characterize the topology of this vector bundle using the Zak phase [43] for the bands. This quantity is a special case of the Berry phase [19,43] to characterize the band topology in 1D periodic media. It is given for the band m by

$$Z = \int_{-\pi}^{\pi} [i(\boldsymbol{A}^{(m)})^H(\mu) \cdot \partial_\mu \boldsymbol{A}^{(m)}(\mu)] d\kappa, \tag{B2}$$

where $(\boldsymbol{A}^{(m)})^H(\mu)$ is the conjugate transpose or Hermitian of the eigenvector $\boldsymbol{A}^{(m)}(\mu)$. For numerical calculations, we use an equivalent discretized form of Eq. (B2) given by [19]

$$\theta^{\text{Zak}} = -\text{Im} \sum_{n=-N}^{N-1} \ln \left[\boldsymbol{A}_m^H\left(\frac{n}{N}\pi\right) \cdot \boldsymbol{A}_m\left(\frac{n+1}{N}\pi\right)\right]. \tag{B3}$$

The Zak phase of both the acoustic and optical bands takes the values $Z = 0$ and $Z = \pi$ for the lattices with $\gamma > 0$ and $\gamma < 0$, respectively. Indeed, it should be noted that since the Zak phase is not gauge-invariant [44], the choice of coordinate reference and unit cell must remain the same for computing this quantity.

To understand the meaning of the Zak phase, we show the behavior of the acoustic mode eigenvector for both $\gamma > 0$ and $\gamma < 0$ lattices. For consistent representation, a gauge is fixed such that the eigenvector has magnitude 1 and its first component is real and positive, i.e., at zero angle in the complex plane. The second component $A_b^{(1)}$ of the eigenvector is displayed in the complex plane for μ varying from $-\pi$ to π; see Figs. 13(c) and 13(d). This component of the eigenvector will form a loop as the wave number μ is varied from $-\pi$ to π. When $\gamma > 0$, this eigenvector loop does not enclose the origin and it leads to a Zak phase equal to 0. On the other hand, the acoustic band of a lattice with $\gamma < 0$ has a Zak phase of $Z = \pi$ and its eigenvector loop $A_b(\mu)$ encloses the origin.

APPENDIX C: EFFECTIVE STIFFNESS OF INTERFACE MASS

We consider a finite lattice with an interface where the masses at both ends are fixed. Using the transfer-matrix relations, we derived the following expression in Appendix A for the equivalent stiffness of the interface mass:

$$\left[2(1+\gamma)\left(1 - \frac{S_{21}}{S_{11}}\right) - \Omega^2\right] u_{c,0} = f,$$

where $\boldsymbol{S} = \boldsymbol{T}^{-N}$. Let us now derive an explicit expression for the terms of the matrix $\boldsymbol{S}$ that appear in the above expression. Let us assume that $\boldsymbol{T}^{-1}$ is diagonalizable. This assumption is verified later by examining its eigenvectors. We now use the following result from linear algebra [45]: there exists a unique decomposition $\boldsymbol{T}^{-1} = \boldsymbol{U}\boldsymbol{D}\boldsymbol{U}^{-1}$, where $\boldsymbol{D}$ is a diagonal matrix having the eigenvalues of $\boldsymbol{T}^{-1}$, and $\boldsymbol{U}$ is a matrix whose columns are the corresponding eigenvectors of $\boldsymbol{T}^{-1}$. We determine this decomposition by solving for the eigenvectors of $\boldsymbol{T}^{-1}$, which then leads to the following expression for $\boldsymbol{S}$:

$$\boldsymbol{S} = \boldsymbol{T}^{-N} = \boldsymbol{U}\boldsymbol{D}^N\boldsymbol{U}^{-1} = [\boldsymbol{U}]\begin{pmatrix} \lambda_1^N & 0 \\ 0 & \lambda_2^N \end{pmatrix}[\boldsymbol{U}^{-1}], \tag{C1}$$

where

$$\lambda_{1,2} = \frac{-2 - 2\gamma^2 + (2-\Omega^2)^2 \pm \Omega\sqrt{(\Omega^2-4)[-4\gamma^2+(2-\Omega^2)^2]}}{2(1-\gamma^2)},$$

$$[\boldsymbol{U}] = \begin{pmatrix} \frac{4\gamma+(2-\Omega^2)^2+\Omega\sqrt{(\Omega^2-4)[-4\gamma^2+(2-\Omega^2)^2]}}{2(1+\gamma)(2-\Omega^2)} & \frac{4\gamma+(2-\Omega^2)^2-\Omega\sqrt{(\Omega^2-4)[-4\gamma^2+(2-\Omega^2)^2]}}{2(1+\gamma)(2-\Omega^2)} \\ 1 & 1 \end{pmatrix}.$$

Note that the term within the square root in the eigenvectors is positive for all frequencies Ω in the band gaps and thus the two eigenvectors are distinct. These two distinct eigenvectors span the vector space $\mathbb{R}^2$ and hence $\boldsymbol{T}^{-1}$ is diagonalizable [45], which verifies the assertion made earlier.

APPENDIX D: ASYMPTOTIC ANALYSIS PROCEDURE

To seek the dispersion relation of the lattice, the governing equation for a lattice unit cell j is written in matrix form as

$$\boldsymbol{M}\ddot{\boldsymbol{u}}_j + \sum_p \boldsymbol{K}_p \boldsymbol{u}_p + f_{\mathrm{NL}}(\boldsymbol{u}_j, \boldsymbol{u}_p) = \boldsymbol{0}. \tag{D1}$$

The displacement and frequency are solved using the method of multiple scales, having the following asymptotic expansions for displacement $\boldsymbol{u}$ and time t:

$$\begin{aligned} \bar{\boldsymbol{u}}_j &= \boldsymbol{u}_j^{(0)} + \epsilon \boldsymbol{u}_j^{(1)} + O(\epsilon^2), \\ t &= \omega\tau = [\omega_0 + \epsilon\omega_1 + O(\epsilon^2)]\tau. \end{aligned} \tag{D2}$$

Assuming $\boldsymbol{u}_j$ is harmonic with frequency ω, and substituting the above equations into the governing equations (Newton's laws), yields the following equations for the various orders of ϵ:

$$\epsilon^0 : \quad \omega_0^2 \boldsymbol{M}\frac{d^2\boldsymbol{u}_m^{(0)}}{d\tau^2} + \sum_p \boldsymbol{K}_p \boldsymbol{u}_{m+p}^{(0)} = 0, \tag{D3}$$

$$\begin{aligned} \epsilon^1 : \omega_0^2 \boldsymbol{M}\frac{d^2\boldsymbol{u}_m^{(1)}}{d\tau^2} + \sum_p \boldsymbol{K}_p \boldsymbol{u}_{m+p}^{(1)} \\ = -2\omega_0\omega_1 \boldsymbol{M}\frac{d^2\boldsymbol{u}_m^{(0)}}{d\tau^2} - \sum_p f_{NL}\left(\boldsymbol{u}_m^{(0)}, \boldsymbol{u}_{m+p}^{(0)}\right). \end{aligned} \tag{D4}$$

The solution of the above equations yields the first-order plane waves and their amplitude-dependent dispersion relations.

The zeroth-order equation is linear and is solved using the Floquet Bloch theory. We impose a traveling-wave solution of the form $\boldsymbol{u}_p^{(0)}(\tau) = z_m e^{i\boldsymbol{\mu}\cdot\boldsymbol{x}_p} e^{i\tau}$, where $\boldsymbol{z}$ is the eigenvector associated with a wave with wave vector $\boldsymbol{\mu}$, $\boldsymbol{x}_p$ is the spatial location of the center of a unit cell with index p, and $\boldsymbol{u}_p^{(0)}$ is the vector with components having the generalized displacement of unit cell p. Substituting this expression into the system of governing equations for a unit cell in Eq. (D3) leads to the eigenvalue problem $\sum_p \boldsymbol{K}_p e^{i\boldsymbol{\mu}\cdot\boldsymbol{x}_p}\boldsymbol{z} = \omega_0^2\boldsymbol{M}\boldsymbol{z}$ for a fixed wave vector $\boldsymbol{\mu}$ in the reciprocal-lattice space. Its solution yields the dispersion surface $\omega = \omega(\boldsymbol{\mu})$ of the zeroth-order linear system. Then the zeroth-order displacement of a cell p due to the mth wave mode, with eigenvector z_m, may be written as

$$\boldsymbol{u}_p^{(0)}(\tau) = \frac{A_0}{2}[z_m(\boldsymbol{\mu})e^{i\boldsymbol{\mu}\cdot\boldsymbol{x}_p}e^{i\tau} + \text{c.c.}], \tag{D5}$$

where c.c. denotes the complex conjugate, A_0 is the wave amplitude, and $z_m(\boldsymbol{\mu})$ is the mth wave mode at the wave vector $\boldsymbol{\mu}$. The eigenvector $z_m(\boldsymbol{\mu})$ is normalized so that the maximum absolute value of any component is 1. Thus the maximum displacement of any mass in the lattice is A_0.

In contrast with linear media, the dispersion behavior of our nonlinear lattice will depend on the amplitude A_0 of the wave mode, and we determine the first-order correction in the dispersion relation as a function of this amplitude. To this end, the first-order equation is solved to get a correction due to the nonlinear terms. Substituting Eq. (D5) into the first-order equation (D3) leads to the following equation corresponding to the jth wave mode:

$$\begin{aligned} \omega_0^2 \boldsymbol{M}\frac{d^2\boldsymbol{u}_m^{(1)}}{d\tau^2} + \sum_p \boldsymbol{K}_{p,m}\boldsymbol{u}_{p+m}^{(1)} \\ = \omega_0\omega_1 A_0 \boldsymbol{M}\boldsymbol{u}_m^{(0)} e^{i\tau} \\ - \sum_p f_{\mathrm{NL}}\left(\boldsymbol{u}_m^{(0)}, \boldsymbol{u}_{m+p}^{(0)}\right) = \boldsymbol{F}(\boldsymbol{\mu}). \end{aligned} \tag{D6}$$

Note that the linear part of Eq. (D6) (terms on the left) is identical to the ϵ^0 order equation [Eq. (D3)]. The term $\boldsymbol{F}(\boldsymbol{\mu})$ on the right-hand side is the additional forcing term in the ϵ^1-order equation due to nonlinear effects. The component of $\boldsymbol{F}$ along $\boldsymbol{u}_j^0$ is identified as a secular term and it should vanish for the ϵ^1 solution to be bounded. This condition may be written as

$$\left(\boldsymbol{u}_j^0, \boldsymbol{F}(\boldsymbol{\mu})\right) = \int_0^{2\pi} \left(\boldsymbol{u}_j^0\right)^H \boldsymbol{F}(\boldsymbol{\mu}) d\tau = 0. \tag{D7}$$

Substituting terms from Eq. (D6) into $\boldsymbol{F}$, the above condition leads to an equation for the first-order frequency correction ω_1. For the jth mode, solving this equation gives

$$\omega_1(A_0, \boldsymbol{\mu}) = \frac{\boldsymbol{u}_m^{(0)H}}{2\pi\omega_{0,j}A_0\boldsymbol{u}_m^{(0)H}\boldsymbol{M}\boldsymbol{u}_m^{(0)}} \int_0^{2\pi} \sum_p f_{\mathrm{NL}} e^{-i\tau} d\tau. \tag{D8}$$

Note that since $\boldsymbol{u}^{(0)}$ is a periodic function of time τ with period 2π, the nonlinear forcing function f_{NL} is also periodic in τ. The nonlinear forces also depend on the amplitude A_0 of the zeroth-order wave mode.

We now address two technical points that ensure the uniqueness of the above expression for $\omega_{1,j}$. The first is when there are repeated eigenvalues, and the second is about the invariance of the correction ω_1 to the scaling of eigenvectors by $e^{i\theta}$. A procedure is outlined to address the case of repeated eigenvalues in a systematic way, which results in a unique and well-defined value of the frequency correction. Let us

consider a wave vector $\boldsymbol{\mu}$ at which there are p repeated eigenvalues ω_0 and the corresponding eigenvectors are $\{\boldsymbol{v}_i : 1 \leqslant i \leqslant p\}$. A linear combination of any of these p eigenvectors is also a valid eigenvector, and these eigenvectors define a vector subspace. However, note that $\boldsymbol{c}_1$ in Eq. (D8) depends on the eigenvectors in a nonlinear way, and hence its value will depend on the choice of eigenvectors from this vector subspace. As an illustrative example, consider the eigenvalues and eigenvectors of the identity $\boldsymbol{I}_2$ matrix. It has a repeated eigenvalue 1, and the corresponding eigenvectors are nonunique. We consider two sets of eigenvectors $(\boldsymbol{v}_1, \boldsymbol{v}_2)$ and $(\boldsymbol{w}_1, \boldsymbol{w}_2)$:

$$\boldsymbol{v}_1 = \begin{pmatrix} 1 \\ 0 \end{pmatrix} e^{i\tau}, \quad \boldsymbol{v}_2 = \begin{pmatrix} 0 \\ 1 \end{pmatrix} e^{i\tau},$$
$$\boldsymbol{w}_1 = \begin{pmatrix} 1/\sqrt{2} \\ 1/\sqrt{2} \end{pmatrix} e^{i\tau}, \quad \boldsymbol{w}_2 = \begin{pmatrix} 1/\sqrt{2} \\ -1/\sqrt{2} \end{pmatrix} e^{i\tau}.$$

Solving for ω_1 gives different values for the $\boldsymbol{v}_i$ and $\boldsymbol{w}_i$ sets as $\boldsymbol{c}_1$ has a nonlinear dependence on the components. To resolve this anomaly, we remark here that the eigenvalue correction corresponds to waves propagating at specific prescribed amplitude A_0. Note that this amplitude is prescribed on distinct eigenvectors in a mutually exclusive manner. For example, if we prescribe the zeroth-order solution displacement on masses (i, j), the eigenvectors $(\boldsymbol{u}_1, \boldsymbol{u}_2)$ having a common eigenvalue should satisfy the constraint

$$v_1(i) = \alpha A_0, \quad v_1(j) = 0, \quad v_2(i) = 0, \quad v_2(j) = \beta A_0, \tag{D9}$$

where α and β are normalizing constants such that the maximum magnitude of any component is unity (i.e., $\|\boldsymbol{v}_1\|_\infty = \|\boldsymbol{v}_2\|_\infty = 1$).

Extending the above observation to the general case having p common eigenvalues with eigenvectors, we present the following approach to get a set of transformed eigenvectors which obey a generalized form of the constraint in Eq. (D9). For each eigenvector $\boldsymbol{u}_i$ in this set of repeated eigenvalues, we find a corresponding transformed eigenvector $\boldsymbol{v}_i$ by setting $p - 1$ components of $\boldsymbol{u}_i$ to zero. These $p - 1$ components are simply chosen to be those that have the highest magnitude. Note that if the indices of these components coincide with those chosen for another i distinct from this set of repeated eigenvalues, then a different set of indices is chosen. This procedure ensures that we are enforcing distinct components to zero to get the orthogonal modes.

The second point about the invariance of $\omega_{1,j}$ to the specific choice of gauge factor $e^{i\theta}$ is explained by noting that only the component corresponding to $e^{i\tau}$ in f_{NL} is relevant to the computation of $\boldsymbol{c}_1$, and the contribution of all other components is zero due to orthogonality. Hence, $\boldsymbol{c}_1$ depends linearly on $e^{i\theta}$, and multiplying by $\boldsymbol{u}^H$, which has a factor $e^{-i\theta}$, ensures that the resulting final expression is independent of θ.

[1] M. I. Hussein, M. J. Leamy, and M. Ruzzene, Dynamics of phononic materials and structures: Historical origins, recent progress, and future outlook, Appl. Mech. Rev. **66**, 040802 (2014).

[2] S. D. Huber, Topological mechanics, Nat. Phys. **12**, 621 (2016).

[3] C. Brendel, V. Peano, O. Painter, and F. Marquardt, Snowflake topological insulator for sound waves, Phys. Rev. B **97**, 020102 (2018).

[4] A. B. Khanikaev, S. H. Mousavi, W.-K. Tse, M. Kargarian, A. H. MacDonald, and G. Shvets, Photonic topological insulators, Nat. Mater. **12**, 233 (2013).

[5] V. Peano, C. Brendel, M. Schmidt, and F. Marquardt, Topological Phases of Sound and Light, Phys. Rev. X **5**, 031011 (2015).

[6] S. H. Mousavi, A. B. Khanikaev, and Z. Wang, Topologically protected elastic waves in phononic metamaterials, Nat. Commun. **6**, 8682 (2015).

[7] R. K. Pal and M. Ruzzene, Edge waves in plates with resonators: An elastic analog of the quantum valley Hall effect, New J. Phys. **19**, 025001 (2017).

[8] N. Swinteck, S. Matsuo, K. Runge, J. O. Vasseur, P. Lucas, and P. A. Deymier, Bulk elastic waves with unidirectional backscattering-immune topological states in a time-dependent superlattice, J. Appl. Phys. **118**, 063103 (2015).

[9] H. Nassar, X. C. Xu, A. N. Norris, and G. L. Huang, Modulated phononic crystals: Non-reciprocal wave propagation and Willis materials, J. Mech. Phys. Solids **101**, 10 (2017).

[10] E. Prodan and C. Prodan, Topological Phonon Modes and Their Role in Dynamic Instability of Microtubules, Phys. Rev. Lett. **103**, 248101 (2009).

[11] L. M. Nash, D. Kleckner, A. Read, V. Vitelli, A. M. Turner, and W. T. M. Irvine, Topological mechanics of gyroscopic metamaterials, Proc. Natl. Acad. Sci. (USA) **112**, 14495 (2015).

[12] A. B. Khanikaev, R. Fleury, S. H. Mousavi, and A. Alù, Topologically robust sound propagation in an angular-momentum-biased graphene-like resonator lattice, Nat. Commun. **6**, 8260 (2015).

[13] R. K. Pal, M. Schaeffer, and M. Ruzzene, Helical edge states and topological phase transitions in phononic systems using bilayered lattices, J. Appl. Phys. **119**, 084305 (2016).

[14] C. He, Z. Li, X. Ni, X. C. Sun, S. Y. Yu, M. H. Lu, X. P. Liu, and Y. F. Chen, Topological phononic states of underwater sound based on coupled ring resonators, Appl. Phys. Lett. **108**, 031904 (2016).

[15] R. Süsstrunk and S. D. Huber, Observation of phononic helical edge states in a mechanical topological insulator, Science **349**, 47 (2015).

[16] J. Ningyuan, C. Owens, A. Sommer, D. Schuster, and J. Simon, Time- and Site-Resolved Dynamics in a Topological Circuit, Phys. Rev. X **5**, 021031 (2015).

[17] E. Prodan, K. Dobiszewski, A. Kanwal, J. Palmieri, and C. Prodan, Dynamical Majorana edge modes in a broad class of topological mechanical systems, Nat. Commun. **8**, 14587 (2017).

[18] R. Chaunsali, A. Thakkar, E. Kim, P. G. Kevrekidis, and J. Yang, Demonstrating an *in Situ* Topological Band Transition in Cylindrical Granular Chains, Phys. Rev. Lett. **119**, 024301 (2017).
[19] M. Xiao, G. Ma, Z. Yang, P. Sheng, Z. Q. Zhang, and C. T. Chan, Geometric phase and band inversion in periodic acoustic systems, Nat. Phys. **11**, 240 (2015).
[20] C. L. Kane and T. C. Lubensky, Topological boundary modes in isostatic lattices, Nat. Phys. **10**, 39 (2014).
[21] J. Paulose, A. S. Meeussen, and V. Vitelli, Selective buckling via states of self-stress in topological metamaterials, Proc. Natl. Acad. Sci. (USA) **112**, 7639 (2015).
[22] D. Z. Rocklin, B. G. Chen, M. Falk, V. Vitelli, and T. C. Lubensky, Mechanical Weyl Modes in Topological Maxwell Lattices, Phys. Rev. Lett. **116**, 135503 (2016).
[23] D. Rocklin, Directional mechanical response in the bulk of topological metamaterials, New J. Phys. **19**, 065004 (2017).
[24] R. Fleury, D. L. Sounas, C. F. Sieck, M. R. Haberman, and A. Alù, Sound isolation and giant linear nonreciprocity in a compact acoustic circulator, Science **343**, 516 (2014).
[25] J. Vila, R. K. Pal, M. Ruzzene, and G. Trainiti, A Bloch-based procedure for dispersion analysis of lattices with periodic time-varying properties, J. Sound Vibr. **406**, 363 (2017).
[26] R. K. Pal and P. H. Geubelle, Wave tailoring by precompression in confined granular systems, Phys. Rev. E **90**, 042204 (2014).
[27] N. Boechler, G. Theocharis, and C. Daraio, Bifurcation-based acoustic switching and rectification, Nat. Mater. **10**, 665 (2011).
[28] A. Alù, Metamaterials: Prime time, Nat. Mater. **15**, 1229 (2016).
[29] Y. Hadad, A. B. Khanikaev, and A. Alù, Self-induced topological transitions and edge states supported by nonlinear staggered potentials, Phys. Rev. B **93**, 155112 (2016).
[30] M. J. Ablowitz, C. W. Curtis, and Y.-P. Ma, Linear and nonlinear traveling edge waves in optical honeycomb lattices, Phys. Rev. A **90**, 023813 (2014).
[31] D. Leykam and Y. D. Chong, Edge Solitons in Nonlinear-Photonic Topological Insulators, Phys. Rev. Lett. **117**, 143901 (2016).
[32] Y. Lumer, Y. Plotnik, M. C. Rechtsman, and M. Segev, Self-Localized States in Photonic Topological Insulators, Phys. Rev. Lett. **111**, 243905 (2013).
[33] M. J. Ablowitz and J. T. Cole, Tight-binding methods for general longitudinally driven photonic lattices: Edge states and solitons, Phys. Rev. A **96**, 043868 (2017).
[34] X. Zhou, Y. Wang, D. Leykam, and Y. D. Chong, Optical isolation with nonlinear topological photonics, New J. Phys. **19**, 095002 (2017).
[35] R. K. Narisetti, M. J. Leamy, and M. Ruzzene, A perturbation approach for predicting wave propagation in one-dimensional nonlinear periodic structures, J. Vibr. Acoust. **132**, 031001 (2010).
[36] R. K. Narisetti, M. Ruzzene, and M. J. Leamy, A perturbation approach for analyzing dispersion and group velocities in two-dimensional nonlinear periodic lattices, J. Vibr. Acoust. **133**, 061020 (2011).
[37] M. Xiao, Z. Q. Zhang, and C. T. Chan, Surface Impedance and Bulk Band Geometric Phases in One-Dimensional Systems, Phys. Rev. X **4**, 021017 (2014).
[38] A. H. Nayfeh, *Perturbation Methods* (Wiley-VCH, Weinheim, Germany, 2008).
[39] L. Verlet, Computer "experiments" on classical fluids. i. Thermodynamical properties of Lennard-Jones molecules, Phys. Rev. **159**, 98 (1967).
[40] M. Z. Hasan and C. L. Kane, Colloquium: Topological insulators, Rev. Mod. Phys. **82**, 3045 (2010).
[41] B. A. Bernevig, T. L. Hughes, and S. C. Zhang, Quantum spin Hall effect and topological phase transition in hgte quantum wells, Science **314**, 1757 (2006).
[42] O. A. Pankratov, S. V. Pakhomov, and B. A. Volkov, Supersymmetry in heterojunctions: Band-inverting contact on the basis of $Pb_{1x}Sn_xTe$ and $Hg_{1x}Cd_xTe$, Solid State Commun. **61**, 93 (1987).
[43] J. Zak, Berry's Phase for Energy Bands in Solids, Phys. Rev. Lett. **62**, 2747 (1989).
[44] M. Atala, M. Aidelsburger, J. T. Barreiro, D. Abanin, T. Kitagawa, E. Demler, and I. Bloch, Direct measurement of the Zak phase in topological Bloch bands, Nat. Phys. **9**, 795 (2013).
[45] K. Hoffman and R. Kunze, *Linear Algebra* (Prentice-Hall, Englewood Cliffs, NJ, 1971).